Molecular catalytic system for efficient water splitting

Joya, K.S.

Chapter 5

Catalytic Electro-assisted Water Splitting by Single Site Iridium Complexes

ABSTRACT

In this chapter, mono iridium complexes of the type $[(Cp^*)\text{-}Ir^{III}\text{-}(N\text{–}N)\text{-}OH_2]^{2+}$ for homogeneous catalytic water oxidation to molecular oxygen as well as surface immobilized electro-driven catalytic water splitting are described. Chloro complexes $[(Cp^*)\text{-}Ir^{III}\text{-}(N\text{–}N)\text{-}Cl]^{+}$ (Cp* is pentamethylcyclopentadiene and N–N is a dinitrogen ligand) were obtained by stirring a reaction mixture of $[IrCl_2(Cp^*)]_2$ with dinitrogen ligands in methanol. By OH_2 exchange in aqueous solution the $[(Cp^*)\text{-}Ir^{III}\text{-}(N\text{–}N)\text{-}OH_2]^{2+}$ complexes are obtained that are activated for water splitting catalysis. For electro-assisted water oxidation catalysis, the $[(bpy)Ir^{III}(Cp^*)OH_2]^{2+}$ catalyst was immobilized on an indium doped tin oxide (ITO) working electrode surface by anchoring groups COOH or PO_3H_2 introduced at the 4,4' positions on the dinitrogen ligand. Controlled-potential water electrolysis generates more than 2.1×10^5 turnovers at a rate of >6.5 moles of oxygen per mole of catalyst per second. This study presents the first example of $[(Cp^*)\text{-}Ir^{III}\text{-}(N\text{–}N)\text{-}OH_2]^{2+}$ type aqua ligated catalysts for water oxidation at an electrode surface.

Based on: K.S. Joya and H.J.M. de Groot, **2011** (*submitted*).

5.1. INTRODUCTION

Although most of the water oxidation catalysis research has been oriented towards ruthenium and manganese complexes with a polypyridyl ligand architecture [1-6], both for homogeneous as well as surface immobilized electrochemical systems [7-13], very recently several iridium based complexes have been introduced that show relatively high turn over frequency (TOF) for oxygen evolution in homogeneous investigations [14,15]. However, the stability and turnover numbers (TON) were not high enough to allow incorporation of the catalyst in light driven electrochemical water splitting devices for fuel generation [16,17].

As it is explained in the preceding chapter, an active oxygen evolving complex has to be immobilized on a conducting surface for application in operational electrocatalytic or light driven water splitting devices, and iridium based molecular complexes are not yet studied in electro-driven systems [18-22]. Brudvig and Crabtree recently described a Cp*-Ir aqua or hydroxo catalyst named "blue layer" that was generated by anodic deposition in a pH=6 aqueous potassium nitrate solution [23]. The catalyst operates with a current density up to 1.4 mA/cm^2 at ~1.4 V (vs. NHE) for water oxidation in 0.1M KNO_3 (pH=6) electrolyte solution. SEM analysis of the electrodeposited matrix reveals a film thickness between 1 and 2 μm, which represents a multilayer deposition on a fluorine-doped tin oxide (FTO) electrode surface and the formation of oxides of iridium cannot be excluded [23,24].

In this chapter, an immobilized catalytic electro-assisted water oxidation assembly using a linker modified L_2bpy-Ir^{III}Cp* complex (L is COOH and PO_3H_2 and bpy is 2,2′-bipyridine) for surface anchoring on an indium-doped tin oxide (ITO) working electrode is described (Fig. 5.1). An ITO surface of 1 cm^2 covered with the catalyst layer generates rapid turnover rate with high TON's for molecular oxygen during controlled-potential water electrolysis [25].

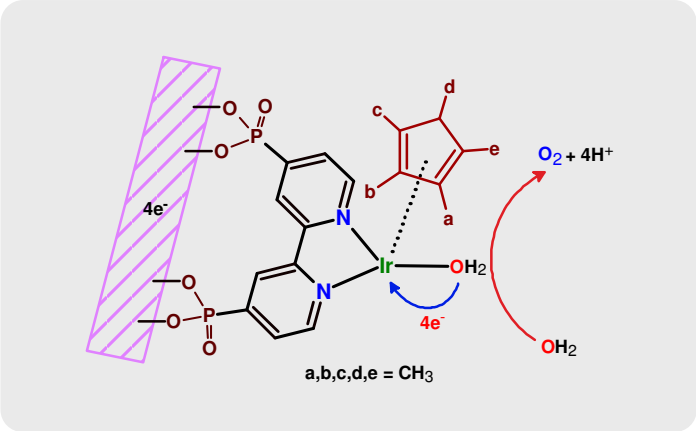

Figure 5.1. Schematic representation of the mono-iridium complex anchored to a conducting oxide surface (ITO) with linker (L = PO_3H_2) for electro-assisted water oxidation.

In addition, three aqua ligated iridium catalysts with different dinitrogen ligands $[(N–N)Ir^{III}(Cp^*)\text{-}OH_2]^{2+}$, analogous to the recently reported chloro or iodo bonded mono iridium complexes [26], are presented here and tested for homogeneous water oxidation studies (Fig. 5.2). While for the earlier examples exchange of a halogen with a neutral water molecule to instigate the water oxidation cycle produces an initial lag phase due to slow dissociation of the halogen from the iridium centre, a faster rate and efficient catalytic activity is observed for the aqua ligated mono iridium complexes described in this chapter [26].

5.2. RESULTS AND DISCUSSION

5.2.1. Catalytic Complexes Synthesis and Characterization

For homogeneous water oxidation catalysis, the iridium catalysts $[(bpy)Ir^{III}(Cp^*)\text{-}OH_2]^{2+}$ (Cat.**Ir**–bpy), $[(phen)Ir^{III}(Cp^*)\text{-}OH_2]^{2+}$ (Cat.**Ir**–phen) and $[(bpm)Ir^{III}(Cp^*)\text{-}OH_2]^{2+}$ (Cat.**Ir**–bpm), are obtained by immersion of the chloro complexes into a water methanol mixture containing silver nitrate or hexafluorophosphate salt (Fig.

5.2). The removal of the Cl^- after aqua induction is important to avoid the involvement of the halogen ions with the water oxidation process [27].

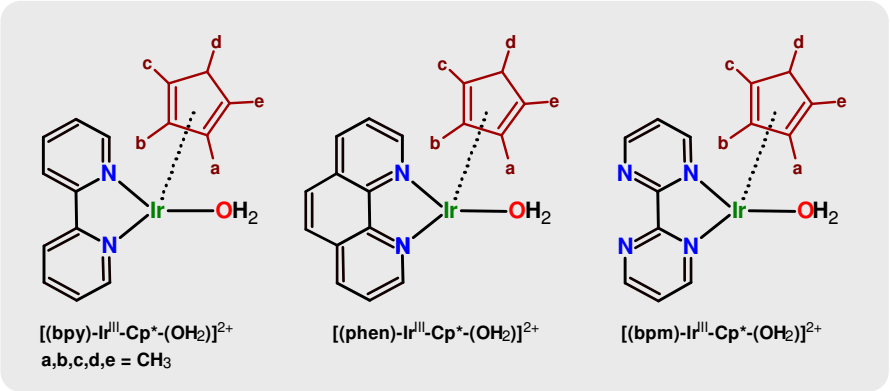

Figure 5.2. Mono iridium pentamethylcyclopentadiene (Cp*) derived 2,2′-bipyridine, phenanthroline (phen) and bipyrimidine (bpm) mono nuclear complexes [25].

The crystal structures of these complexes reveal a large bite angle of the iridium center with respect to the dinitrogen ligand and the aromatic Cp*. This possibly facilitates the aqua exchange at the iridium catalytic site and provides a wide gap for OH_2 coordination between the bpy-Ir and the cyclic conjugated hydrocarbon [25]. The strong electron donating character of the Cp* ligand helps to prevent the formation of higher oxidation iridium intermediates during the catalytic cycle [26].

The linker modified complexes with COOH and PO_3H_2 units at the 4,4′-positions in the $[(bpy)Ir^{III}(Cp^*)Cl]^+$ complex and the $[(bpy)Ir^{III}(Cp^*)\text{-}OH_2]^{2+}$ catalyst for electrochemical water oxidation were synthesized by stirring the mixture of the H_2dcabpy (4,4′-dicarboxylic acid-2,2′-bipyridine) or the H_4dphbpy (4,4′-diphosphonic acid-2,2′-bipyridine) ligand with $[IrCl_2(Cp^*)]_2$ dimer. The chloro complexes thus obtained are transformed into $[(H_2dcabpy)Ir^{III}(Cp^*)\text{-}OH_2]^{2+}$ (Cat.**Ir**–COOH) and $[(H_4dphbpy)Ir^{III}(Cp^*)\text{-}OH_2]^{2+}$ (Cat.**Ir**–PO_3H_2) by stirring with aqueous silver hexafluorophosphate salt or $AgNO_3$ in methanol. (see synthesis detail, ^{1}H-NMR and elemental analysis in section 5.4). *In situ* aqua exchange of the

chloro complex and deprotonation to form the $[(bpy)Ir^{III}(Cp^*)\text{-}OH]^{2+}$ complex was followed by UV-vis studies (Fig. A5.2).

5.2.2. Cyclic Voltammetry and Homogeneous Water Oxidation

Unlike the single-site ruthenium complexes discussed in the previous chapters, the electrochemistry of the mono iridium catalysts shows no apparent pH dependence of the overpotential for oxygen evolution even in alkaline media pH > 7 with the catalyst in contact with the glassy carbon electrode (Fig. A5.3). It was recently postulated that for the catalysts $[(Cp^*)\text{-}Ir^{III}\text{-}(N–C)\text{-}Cl]^+$ and $[(Cp^*)\text{-}Ir^{III}\text{-}(N–N)\text{-}Cl]^+$ (where N–C is phenyl-pyridine and N–N is bipyridine), the iridium oxidation into $[Ir^{IV}\text{-}(OH)]^{2+}/[Ir^{III}\text{-}(OH_2)]^{2+}$ and $[Ir^{V}{=}O)]^{2+}/[Ir^{IV}\text{-}(OH)]^{2+}$ redox couples is proceeded by two consecutive proton coupled electron transfer (PCET) steps [26]. For catalyst Cat.**Ir**–COOH, the weak polarization signals for the first two redox transitions are ascribed to slow electrode kinetics of the complexes under electrochemical conditions, also at a higher scan rate [28]. At pH > 9, a current wave appears at *ca*. 1.19 V (vs. NHE), which grows with increasing pH at the same potential (Figure A5.3). This catalytic wave apparently indicates current flow leading to water oxidation but, for better understanding, the catalyst was immobilized on an ITO electrode for electro-driven water oxidation and oxygen evolution studies (5.2.3).

The three aqua iridium complexes Cat.**Ir**–bpy, Cat.**Ir**–phen and Cat.**Ir**–bpm were tested for homogeneous water oxidation using an excess amount of Ce(IV) salt. The oxygen evolution was monitored in an airtight glass cell using an oxygen electrode as mentioned in chapter 3. The catalysis initiates within seconds after the addition of the primary oxidant Ce(IV). The $[(bpy)Ir^{III}(Cp^*)\text{-}OH_2]^{2+}$ and $[(phen)Ir^{III}(Cp^*)\text{-}OH_2]^{2+}$ complexes show a rapid initial rate for oxygen formation, faster than the bipyrimidine catalyst (Fig. 5.3). This nicely shows how aqua induction can shorten the initial lag time of this system. For the aqua bonded mono iridium complexes the rates are twice as high as for the halogen derivatives [26]. The oxygen evolution rate attains its maximum value within 1-2 minutes, and afterwards it starts to decrease slowly (Fig. 5.3).

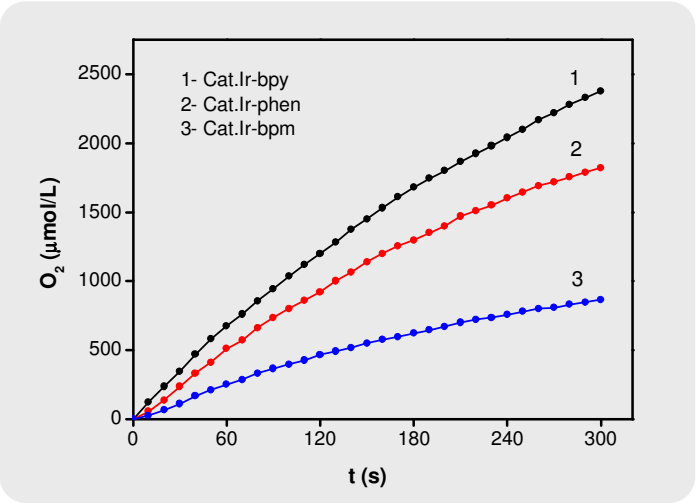

Figure 5.3. Initial oxygen evolution during homogeneous water oxidation catalyzed by (1) $[(bpy)Ir^{III}(Cp^*)\text{-}OH_2]^{2+}$, (2) $[(phen)Ir^{III}(Cp^*)\text{-}OH_2]^{2+}$ and (3) $[(bpm)Ir^{III}(Cp^*)\text{-}OH_2]^{2+}$ complexes in deoxygenated 0.1 M HNO_3 aqueous solutions in the presence of Ce(IV). (Catalysts concentration 25±0.2 µmol/L, Ce(IV) 50 mM).

Similar behaviour is also seen for $[(Cp^*)\text{-}Ir^{III}\text{-}(phpy)\text{-}Cl]^+$, $[(Cp^*)\text{-}Ir^{III}\text{-}(bpy)\text{-}Cl]^+$ and $[(Cp^*)\text{-}Ir^{III}\text{-}(bpy)\text{-}I]^+$ catalysts attributed to oxidation of the complex, including the possible degradation of the nitrogen ligand or the Cp* methyl groups. The TOF for Cat.**Ir**–bpy and Cat.**Ir**–phen is much higher than for the recently reported mono site iridium catalysts [26,29]. Table 5.1 shows a list of the TOF's measured for the first hour and the TON's obtained during five hours of catalysis operation for Cat.**Ir**–bpy, Cat.**Ir**–phen and Cat.**Ir**–bpm. The turnovers for all three systems are at least two times higher than for the fastest $[(bpy)Ir(Cp)\text{-}I]^+$ complex [26]. For prolonged water oxidation catalysis for 5 hours, $[(bpy)Ir^{III}(Cp^*)\text{-}OH_2]^{2+}$ shows a TON of 1500, which is much higher than the chloro and iodo analogues and confirms the increased durability of the catalysis process (Table 5.1). The initial rate of oxygen evolution for the aqua complexes $[(phen)Ir^{III}(Cp^*)\text{-}OH_2]^{2+}$ and $[(bpm)Ir^{III}(Cp^*)\text{-}OH_2]^{2+}$ is 21 and 11.2 min^{-1} respectively, also higher than for the chloro derivative (Table 5.1). It also shows a superior performance of the Ir complexes for homogeneous catalysis compared with the Ru catalysts discussed in chapter 3.

Table 5.1. Rates for oxygen generation and TON's for $[(bpy)Ir^{III}(Cp^*)\text{-}OH_2]^{2+}$, $[(phen)Ir^{III}(Cp^*)\text{-}OH_2]^{2+}$ and $[(bpm)Ir^{III}(Cp^*)\text{-}OH_2]^{2+}$ aqua complexes.

Catalyst	Rate $molO_2$ /(molCat · t)		TON[c] ($molO_2$/molCat)	*Ref.*
	(t.o.min^{-1})[a]	(t.o.hr^{-1})[b]		
Cat.**Ir**–bpy	27	419	>1500/5 hrs	*This work*
Cat.**Ir**–phen	21	301	>1045/5 hrs	*This work*
Cat.**Ir**–bpm	11.2	181	>781/5 hrs	*This work*
[(N-C)Ir(Cp*)-Cl	10	155	349/8 hrs	*26*
[(bpy)Ir(Cp*)-Cl]Cl	14.4	93	320/8 hrs	*26*
[(bpy)Ir(Cp)-I]NO_3	9.3	214	738/8 hrs	*26*
[(phen)Ir(Cp*)-Cl]Cl	8.4	–	–	*26*
[(bpm)Ir(Cp*)-Cl]Cl	3.9	–	–	*26*

[a] initial rate for the oxygen evolution measured for the first 5 minutes; [b] total turnovers (t.o.) obtained in the first hour of catalysis operation and [c] total turnover number obtained during 5 hours of the water oxidation reaction. Catalyst concentration 25±0.2 μmol/L, Ce(IV) 50 mM. The oxygen evolution was monitored *in situ* in an air-tight glass cell using a calibrated oxygen electrode connected to a digital oxy-meter in deoxygenated 0.1 M HNO_3 aqueous solutions.

5.2.3. Oxygen Evolution by Surface Anchored Mono-Iridium Catalysts

The current-potential behaviour of the ITO functionalized catalyst system shows the oxygen onset current wave above 1.5 V (vs. NHE), both in 0.1 M aqueous HNO_3 and in pH=7.35 buffer solutions (Fig. A5.4). This suggests that the rate limiting step is a non PCET mechanism that retains the water oxidation potential above 1.5 V even at higher pH. A polarization current wave appears at *ca*. 1.33 V (vs. NHE) in aqueous acids leading towards oxygen evolution currents (Fig. 5.4). It is followed by a broader reduction wave around 1.27 V during the reverse scan. On the other hand in neutral buffer solution, a polarization wave appears at ca. 0.9 V and is followed by a reversible and an irreversible reduction wave, while the onset of the oxygen current remains above 1.55 V vs. NHE (Fig. 5.4). The single wave in the acidic electrolyte can be assigned to the $[Ir^{IV}\text{-}(OH)]^{2+}/[Ir^{III}\text{-}(OH_2)]^{2+}$ and $[Ir^{V}(=O)]^{2+}/[Ir^{IV}\text{-}(OH)]^{2+}$ transitions occurring in a single step of simultaneous removal of two electrons and two protons which has been reported recently for the

ruthenium analogue $[(terpy)Ru^{II}(bpm)\text{-}OH_2]^{2+}$, where $[Ru^{III}\text{-}OH]^{2+}$ is a "missing" oxidation state [30]. Alternatively, two oxidations of the iridium centre $[Ir^{III}\text{-}OH_2]^{2+}$ can occur at almost the same energy, as described by Brudvig [26].

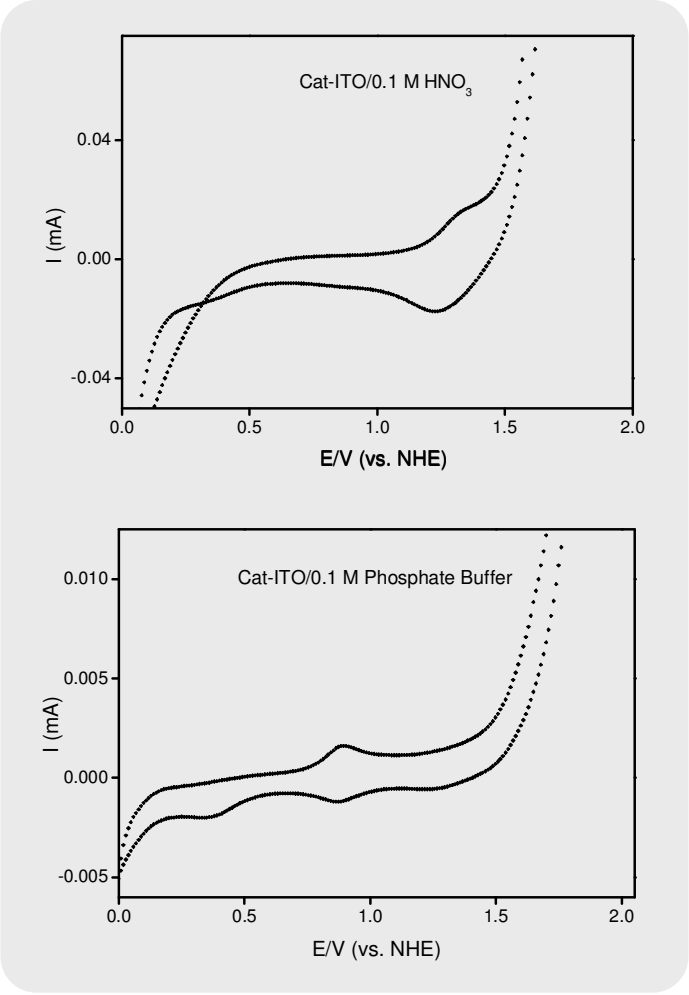

Figure 5.4. Expanded cyclic voltammetry for the $[(H_4dphbpy)\text{-}Ir^{III}\text{-}(Cp^*)]^{2+}$ complex anchored on an ITO electrode in deoxygenated aqueous **(top)** 0.1 M HNO_3 and **(bottom)** 0.1 M phosphate buffer solution (pH=7.35). (Scan rate 50 mV/sec, ITO area A= 1 cm^2).

Oxygen bubbles were also observed on the Cat-ITO working electrode during potential cycling in aqueous solution. The current does not grow by repeating the scans, indicating that there is no apparent electro-deposition of the catalyst or

oxides of iridium in the electrochemical conditions [17]. Following the CV experiments, the Cat.**Ir**–COOH and Cat.**Ir**–PO_3H_2 modified ITO electrodes were used to perform controlled potential catalytic water electrolysis experiments in aqueous solution. An electrolysis cell with separate anodic and cathodic compartments was employed to collect the oxygen and hydrogen as mentioned in the previous chapter. Oxygen evolution was monitored *in situ* with a calibrated oxygen electrode connected with a digital O_2 meter (YSI, Inc., Model 550A).

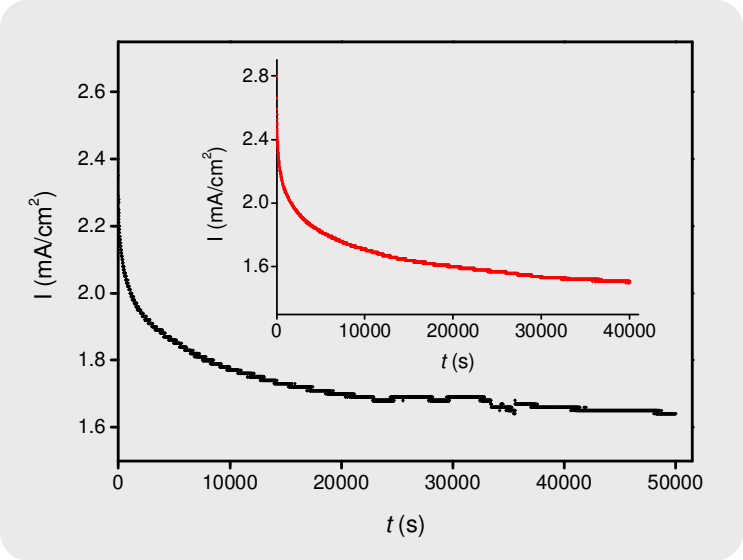

Figure 5.5. Controlled-potential water electrolysis with the Cat.**Ir**–PO_3H_2 modified ITO electrodes in deoxygenated aqueous 0.1 M pH=4 buffer solution, at *ca.* 1.75 V (vs. NHE). Inset shows electrolysis with the Cat.**Ir**–COOH modified ITO electrodes in deoxygenated aqueous solution under similar conditions at *ca.* 1.75 V (vs. NHE), ITO area A= 1 cm^2, (catalyst loading ~1.55–1.70 × 10^{-10} mol/cm^2).

Controlled-potential electrolysis of an aqueous solution with Cat.**Ir**–COOH and Cat.**Ir**–PO_3H_2 modified ITO electrodes were conducted at *ca.* 1.75 V (vs. NHE). Figure 5.5 shows the current-time plots for the catalytic water electrolysis at pH=4. The current densities at 1.75 V (vs. NHE) under steady state conditions were more than 1.61 mA/cm^2 and 1.67 mA/cm^2 for the Cat.**Ir**–COOH and Cat.**Ir**–PO_3H_2 modified ITO respectively. The oxygen generation current densities remain above

1.6 mA/cm^2 for several hours, both for Cat.**Ir**–COOH and for Cat.**Ir**–PO_3H_2 catalyst, and no significant decrease in the catalytic activity was observed. The initial average current densities related to the initial rate of oxygen generation were above >1.8 mA/cm^2 for Cat.**Ir**–PO_3H_2 and more than 1.7 mA/cm^2 for the Cat.**Ir**–COOH modified ITO systems (Fig. A5.5). As the potential is switched on, the oxygen bubble formation from the catalyst modified ITO started within seconds of the catalytic electrolysis operation.

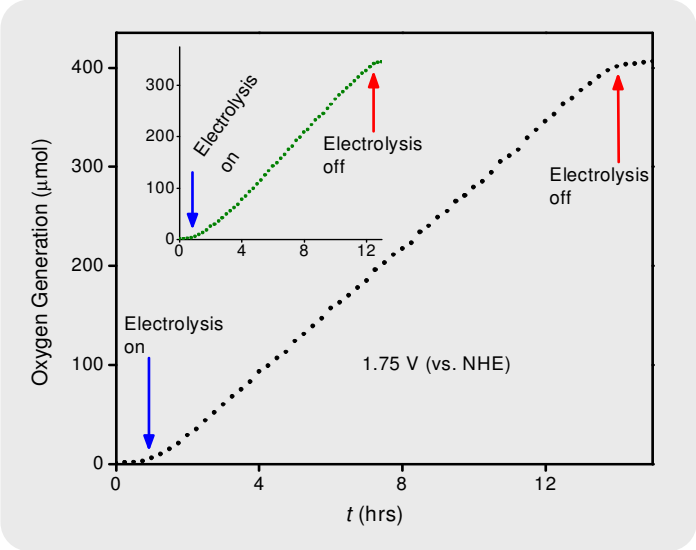

Figure 5.6. Oxygen generation (µmol) vs. time plot for the controlled-potential water electrolysis with Cat.**Ir**–PO_3H_2 modified ITO electrode and (inset) for Cat.**Ir**–COOH modified ITO electrode in deoxygenated aqueous 0.1 M buffer solution (pH=4) over an extended period of 14 hrs at *ca.* 1.75 V (vs. NHE). The blue arrows indicate the beginning of electrolysis and red arrows point to the termination. ITO area A=1 cm^2, (catalyst loading ~1.55–1.70 × 10^{-10} mol/cm^2 for Cat.**Ir**–PO_3H_2 and Cat.**Ir**–COOH).

An affluent stream of oxygen bubbles was leaving the catalyst modified ITO surface along with simultaneous hydrogen generation at the spiral Pt in the cathodic compartment during the electro-assisted catalysis. The Cat.**Ir**–PO_3H_2 modified ITO was found to be as efficient as the Ru based electrocatalytic systems for water electrolysis described in chapter 4, showing more than 1.65 mA/cm^2 oxygen generation current densities for 14 hours of uninterrupted electrolysis (Figs. 5.5-

5.6). In addition, the current densities for both catalytic systems are more than an order of magnitude larger than for the recently reported $–CH_2$-PO_3H_3 modified mono site ruthenium based electrocatalytic water splitting assemblies [13].

During controlled-potential electrolysis at pH=4, the Cat.**Ir**–PO_3H_2 modified ITO system generates more than 400 μmol of molecular oxygen in 13 hours of catalytic operation (Fig. 5.6). The electrolysis was undertaken at *ca.* 1.75 V (vs. NHE) with a stable current density (Fig. 5.5). A rich stream of oxygen is coming out of the Cat.**Ir**–PO_3H_2 modified ITO electrode at a rate of ~6.5 moles of oxygen per mole of catalyst per second. The catalytic system generates more than 2.1×10^5 turnovers for molecular oxygen in 13 hours. This implies that the surface bound iridium half sandwiched molecular catalyst Cat.**Ir**–PO_3H_2 exhibits a superior catalytic performance compared to the anodically deposited Cp*-Ir catalyst [23]. The Cat.**Ir**–COOH modified ITO electrode produces more than 300 μmol of molecular oxygen in 12 hours of controlled-potential electrolysis (inset Fig. 5.6). The current densities were only ~0.05 mA/cm^2 less than those for the Cat.**Ir**-PO_3H_2 modified ITO system at *ca.* 1.75 V potential (vs. NHE).

5.2.4. Water Oxidation and Oxygen Evolution Mechanism

It was recently described for $[(Cp^*)\text{-}Ir^{III}\text{-}(N–C)\text{-}OH_2]^+$ and $[(Cp^*)\text{-}Ir^{III}\text{-}(N–N)\text{-}OH_2]^{2+}$ complexes that the mono iridium-oxo species $[Ir^V{=}O)]^{n+}$ (n=1 for N–C and n=2 for N–N) are generated by two step oxidation of the $[Ir^{III}\text{-}(OH_2)]^{n+}$ with simultaneous proton removal. The important point is the O–O bond formation, possibly by the nucleophilic attack of a OH_2 molecule to the $[Ir^V{=}O)]^{n+}$ complex. At the same time, a proton is thought to leave from the arriving water molecule to make a hydroxide ion that enhances the nucleophilicity for the attack at the oxo complex [26]. The CV's presented in the above section (Fig. 5.4) point to a mechanism where, after the second aqua insertion, the next step of electron removal is not coupled with the proton transfer and *vice versa*, as the oxygen onset potential is not following the pH dependence according to the Nernst law.

Scheme 5.1. Proposed hexacyclic catalytic mechanism for electro-assisted water oxidation and dioxygen formation by the mono iridium $[(N–N)Ir^{III}(Cp^*)\text{-}OH_2]^{2+}$ complex derived from the electrochemistry measurements. Red and green arrows represent the four electron and proton removal events, respectively. The $[(Ir^{III}–O(OH)]^{+}$ and $[(Ir^{IV}–O(OH)]^{2+}$ complexes are generated via consecutive proton transfer and electron removal steps, respectively, on second water insertion. Path (2) is proceeded without the formation of the intermediate $[(Ir^{IV}–(OO)]^{2+}$ and makes a pentacycle reaction route.

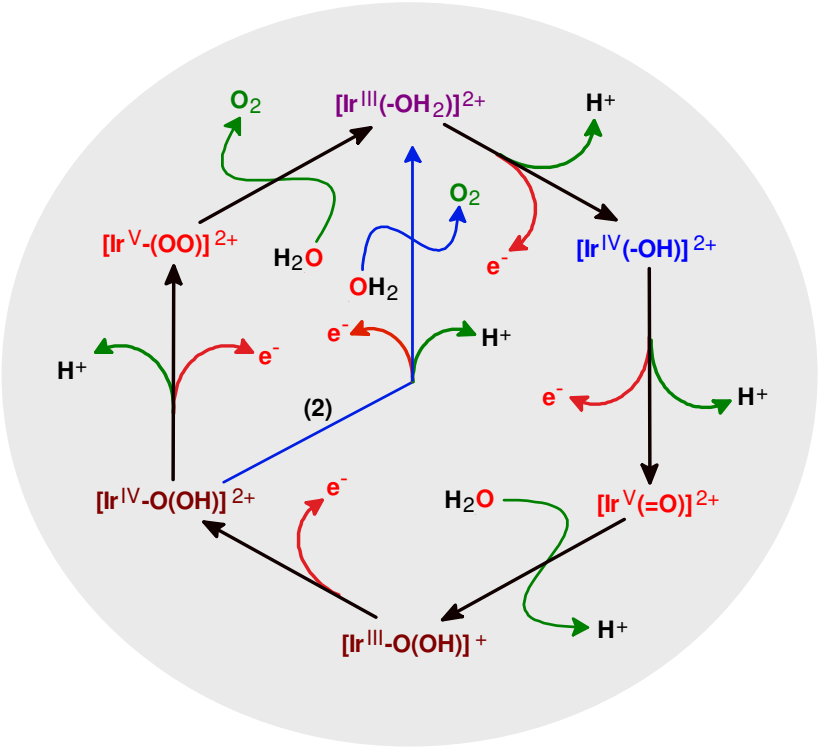

Probably a proton is removed during the second water insertion to the complex $[Ir^{V}=O)]^{n+}$ to generate a $[Ir^{III}–OOH)]^{n+}$ type intermediate with a charge n–1. This can lose two electrons and a proton and generate dioxygen while re-coordinating to another OH_2 to recharge the aqua complex for the next catalytic water oxidation cycle [26]. To enable the possibility of the electron and proton transfer in two steps, most likely the $[Ir^{III}–OOH)]^{n+}$ complex is formed by deprotonation accompanying the second aqua ligation of the complex. When this ejects an electron a $[Ir^{IV}–OOH)]^{n+1}$ type intermediate can be formed in the next step (Scheme 5.1). As the catalyst shows a fast rate for oxygen evolution, the OH_2 ligation may not be the

limiting factor. Most probably the small switchable Cp* provides space for a facile aqua insertion at the beginning of the second half of the water oxidation cycle. In the last step of the mechanism proposed in scheme 5.1, the fourth electron is removed along with a proton release with simultaneous water molecule insertion and dioxygen generation, thereby regenerating the $[Ir^{III}\text{-}(OH_2)]^{n+}$ complex for the next catalytic operation of water oxidation.

5.3. CONCLUSIONS

Stable and easy accessible mono iridium Cp* aqua catalysts $[(bpy)Ir^{III}(Cp^*)\text{-}OH_2]^{2+}$ (Cat.**Ir**–bpy), $[(phen)Ir^{III}(Cp^*)\text{-}OH_2]^{2+}$ (Cat.**Ir**–phen) and $[(bpm)Ir^{III}(Cp^*)\text{-}OH_2]^{2+}$ (Cat.**Ir**–bpm), are developed for homogeneous oxygen evolution. The catalysts avoid the initial lag time for water oxidation and show higher catalytic activity and rate during 5 hours operation than the chloro and iodo derivatives reported recently [26]. The linker modified iridium catalysts are electrocatalytically active and robust when tethered to an ITO electrode surface by anchoring groups (PO_3H_2 or COOH). Cat.**Ir**–PO_3H_2 and Cat.**Ir**–COOH modified ITO electrodes were able to generate molecular oxygen for more than 12 hours of operation without significant loss of activity during controlled-potential water electrolysis. The overall catalyst turnover numbers were more than 2.1×10^5 in 13 hours at a turnover rate of ~6.5 moles of oxygen per mole of catalyst per second. The initial average current densities were more than 1.7 mA/cm^2. This study helps to pave the way for photo-electrocatalytic devices with immobilized mono iridium complexes for future fuel generation from water splitting.

5.4. MATERIALS AND METHODS

Synthesis of the compounds, ligands and complexes was conducted in an argon/nitrogen atmosphere. ITO coated glass slides (10 cm × 2.5 cm), the iridium dimer $[IrCl_2(Cp^*)]_2$ and the ligands 2,2′-bipyridine (bpy) 2,2′-bipyrimidine (bpm), and 1,10-phenanthroline (phen) were obtained from Sigma-Aldrich Co., and used

as received. 4,4′-dicarboxylic acid-2,2′-bipyridine (H_2dcabpy) and 4,4′-diphosphonic acid-2,2′-bipyridine (H_4dphbpy) were obtained as described in chapters 4.

Solutions for electrochemical investigations were prepared in ultra-pure water (Millipore MilliQ® A10 gradient, 18.2 MΩ cm, 2–4 ppb total organic content). All electrochemical measurements were carried out in carefully Ar-purged deoxygenated aqueous solutions at room temperature. Cyclic voltammetry and controlled-potential water oxidation experiments are conducted in a three electrode configuration pyrex glass cell. The potentiostat, working, counter and reference electrodes are the same as described in chapters 3 and 4. The electrode preparation, degassing of the aqueous solution, catalyst loading on ITO slides and *in situ* oxygen measurement are the same as described in the previous chapter.

Synthesis

5.4.1. Chloro Complex [(bpy)Ir^{III}(Cp*)-Cl]Cl (**Ir**–bpy)

2,2′-bipyridine (bpy: 0.156 g, 1.0 mmol) in MeOH (10 mL) was added to a stirred mixture of $[IrCl_2(Cp^*)]_2$ dimer (0.399 g, 0.5 mmol) in ab. MeOH (15 mL). The mixture was further stirred for 1 hour at 40-45 °C. The solution was filtered with a sintered funnel of fine porosity and the solvent was evaporated under vacuum. The solid yellow complex [(bpy)Ir^{III}(Cp*)-Cl]Cl thus obtained was re-precipitated from acetone or MeOH by addition of ether/hexane. Yield 0.37 g, 66 %. ^{1}H NMR (CD_3OD, 295 K, δ ppm, *J* Hz): 8.99 (d, 2H, $H^{6,6'}{}_{bpy}$, *J* 5.41); 8.64 (d, 2H, $H^{3,3'}{}_{bpy}$, *J* 8.11); 8.28 (t, 2H, $H^{4,4'}{}_{bpy}$, *J* 7.92); 7.85 (t, 2H, $H^{5,5'}{}_{bpy}$, *J* 6.66); 1.72 (s, 15H, $CH_3{}^{1\text{-}5}{}_{Cp^*}$), Analysis found: C, 43.24%; H, 4.85%; N, 5.0%. Calculated: C, 43.24%; H, 4.35%; N, 5.04% for $C_{20}H_{24}N_2Ir_1Cl_2$ complex.

5.4.2. Chloro Complex [(phen)Ir^{III}(Cp*)-Cl]Cl (**Ir**–phen)

The bright yellow chloro complex [(phen)Ir^{III}(Cp*)-Cl]Cl was prepared in a similar manner as described above (section 5.4.1) using 1,10-phenanthroline (phen: 0.18 g, 1.0 mmol) instead of 2,2′-bipyridine. Yield 0.39 g, 67 %. ^{1}H NMR (CD_3OD, 295

K, δ ppm, *J* Hz): 9.37 (dd, 2H, $H^{2,9}{}_{phen}$, *J* 1.20, *J* 5.31); 8.87 (dd, 2H, $H^{4,7}{}_{phen}$, *J* 1.20, *J* 8.29); 8.28 (s, 2H, $H^{5,6}{}_{phen}$); 8.18 (dd, 2H, $H^{3,8}{}_{phen}$, *J* 5.25, *J* 8.73); 1.80 (s, 15H, $CH_3{}^{1\text{-}5}{}_{Cp^*}$), Analysis found: C, 43.52%; H, 4.47%; N, 4.71%. Calculated: C, 44.22%; H, 4.39%; N, 4.70% for $C_{22}H_{24}N_2Ir_1Cl_2.H_2O$ complex.

5.4.3. Chloro Complex [(bpm)Ir^{III}(Cp*)-Cl]Cl (**Ir**–bpm)

The yellow chloro complex [(bpm)Ir^{III}(Cp*)-Cl]Cl was prepared in similar manner as described above (section 5.4.1) using 2,2′-bipyrimidine (bpm: 0.158 g, 1.0 mmol) instead of 2,2′-bipyridine. Yield 0.31 g, 55 %. ^{1}H NMR (CD_3CN, 295 K, δ ppm, *J* Hz): 9.27 (dd, 2H, $H^{6,6'}{}_{bpm}$, *J* 2.03, *J* 4.85); 9.11 (dd, 2H, $H^{4,4'}{}_{bpm}$, *J* 2.03, *J* 5.85); 7.92 (t, 2H, $H^{5,5'}{}_{bpm}$, *J* 5.31); 1.70 (s, 15H, $CH_3{}^{1\text{-}5}{}_{Cp^*}$), Analysis found: C, 36.30%; H, 4.33%; N, 9.73%. Calculated: C, 37.56%; H, 4.20%; N, 9.73% for $C_{18}H_{22}N_4Ir_1Cl_2.H_2O$ complex.

5.4.4. Chloro complex [(H_2dcabpy)Ir^{III}(Cp*)Cl]Cl (**Ir**–COOH)

To a mixture of [Ir^{III}(Cp*)(Cl_2)]$_2$ dimer (0.399 g, 0.5 mmol) in ab. MeOH (15 mL) stirred for 15 minutes under argon, 4,4′-dicarboxylic acid-2,2′-bipyridine (H_2dcabpy: 0.244 g, 1.0 mmol) in 0.5 mL water containing NaOH (0.08 g, 2.0 mmol), was slowly added. The mixture was further stirred for 3 hours at 45-50 °C. The solution was cooled to room temperature and the pH was lowered to 1-2 by addition of 0.5 M HCl. The free ligand was filtered off and the solvent mixture was evaporated under vacuum. The solid yellow chloro complex [(H_2dcabpy)Ir^{III}(Cp*)Cl]Cl thus obtained was re-precipitated from MeOH or acetone by addition of ether/hexane. Yield 0.39 g, 61 %. ^{1}H NMR (CD_3OD, 295 K, δ ppm, *J* Hz): 8.99 (d, 2H, $H^{6,6'}{}_{dcabpy}$, *J* 5.79); 8.95 (s, 2H, $H^{3,3'}{}_{dcabpy}$); 8.17 (dd, 2H, $H^{5,5'}{}_{dcabpy}$, *J* 1.59, *J* 5.80); 1.71 (s, 15H, $CH_3{}^{1\text{-}5}{}_{Cp^*}$), Analysis found: C, 36.59%; H, 3.66%; N, 4.0%. Calculated: C, 37.88%; H, 4.33%; N, 4.02% for $C_{22}H_{24}N_2O_4Ir_1Cl_2.3H_2O$ complex.

5.4.5. Chloro complex [$(H_4$dphbpy$)Ir^{III}(Cp^*)Cl]Cl$ (**Ir**–PO_3H_2)

The chloro complex [$(H_4$dphbpy$)Ir^{III}(Cp^*)Cl]Cl$ was prepared in a similar manner as described above (section 5.4.4) using 4,4′-diphosphonic acid-2,2′-bipyridine (H_4dphbpy: 0.316 g, 1.0 mmol) in 0.5 mL water containing NaOH (0.16 g, 4.0 mmol) instead of 4,4'-dicarboxylic acid-2,2′-bipyridine. Yield 0.40 g, 56 %. ^{1}H NMR (CD_3OD, 295 K, δppm, J Hz): 9.02 (s, 2H, $H^{3,3'}{}_{dphbpy}$); 8.80 (d, 2H, $H^{6,6'}{}_{dphbpy}$, J 6.09); 8.08 (dd, 2H, $H^{5,5'}{}_{dphbpy}$, J 2.01, J 6.15); 1.72 (s, 15H, $CH_3{}^{1\text{-}5}{}_{Cp^*}$), Analysis found: C, 32.11%; H, 3.14%; N, 4.10%. Calculated: C, 33.57%; H, 3.66%; N, 3.92% for $C_{20}H_{26}N_2O_6P_2IrCl_2$ complex.

5.4.6. General Synthesis of the Catalyst Complexes:

The mono iridium chloro complexes $[(L)Ir^{III}(Cp^*)\text{-}Cl]^+$ were converted into aqua catalysts $[(L)Ir^{III}(Cp^*)\text{-}OH_2]^{2+}$ by stirring in a water methanol mixture (1:1) containing (2.1 mmol) silver nitrate or hexafluorophosphate salt for 35 minutes at 40-50 °C. The white precipitates were filtered off and the solvent mixture was evaporated under vacuum. The solid bright yellow aqua complexes $[(bpy)Ir^{III}(Cp^*)\text{-}OH_2]^{2+}$, $[(phen)Ir^{III}(Cp^*)\text{-}OH_2]^{2+}$, $[(bpm)Ir^{III}(Cp^*)\text{-}OH_2]^{2+}$ $[(H_2dcabpy)Ir^{III}(Cp^*)\text{-}OH_2]^{2+}$ and $[(H_4dphbpy)Ir^{III}(Cp^*)\text{-}OH_2]^{2+}$ thus obtained were recrystallized from MeOH or acetone by addition of ether/hexane. The aqua exchange was monitored by following the colour change of the solution from orange to yellow visually or by UV-Vis spectral investigation (Fig. A5.2).

REFERENCES

01- M. Calvin, *Science* **1974**, *184*, 375–381.

02- E. L. Lebeau, S. A. Adeyemi and T. J. Meyer, *Inorg. Chem.* **1998,** *37,* 6476–6484.

03- R. Rarnaraj, A. Kira and M. Kaneko, M. *Angew. Chem. Int. Ed. Engl*. **1986,** *25*, 1009–1011.

04- F. P. Rotzinger, S. Munavalli, P. Comte, J. K. Hurst, M. Graetzel, F.-J. Pern and A.J. Frank, *J. Am. Chem. Soc*. **1987**, *109*, 6619–6623.

05- J. Limburg, J. S. Vrettos, L. M. Liable-Sands, A. L. Rheingold, R. H. Crabtree and G.W. Brudvig, *Science* **1999**, *283*, 1524–1527.

06- J. K. Hurst, *Coord. Chem. Rev*. **2005**, *249*, 313–328.

07- J. P. McEvoy and G. W. Brudvig, *Chem. Rev*. **2006,** *106*, 4455–4483.

08- Y. Naruta, M. Sasayama and T. Sasaki, *Angew. Chem. Int. Ed*. **1994**, *33*, 1839–1841.

09- M. Yogi and K. Narita, *J. Am. Chem. Soc*. **2004**, *126*, 8084–8085.

10- X. Sala, I. Romero, M. Rodríguez, L. Escriche and Antoni Llobet, *Angew. Chem. Int. Ed. Engl*. **2009**, *48*, 2842–2852.

11- Z. Chen, J. J. Concepcion, J. W. Jurss and T. J. Meyer, *J. Am. Chem. Soc*. **2009**, *131*, 15580–15581.

12- L. Tong, L. Duan, Y. Xu, T. Privalov and L. Sun, *Angew. Chem. Int. Ed*. **2011**, *50*, 445–449.

13- S. W. Kohl, L. Weiner, L. Schwartsburd, L. Konstantinovski, L. J. W. Shimon, Y. Ben-David, M. A. Iron and D. Milstein. *Science* **2009**, *324*, 74–77.

14- N. D. McDaniel, F. J. Coughlin, L. L. Tinker and S. Bernhard, *J. Am. Chem. Soc*. **2008**, *130*, 210–217.

15- J. F. Hull, D. Balcells, J. D. Blakemore, C. D. Incarvito, O. Eisenstein, G. W. Brudvig and R. H. Crabtree, *J. Am. Chem. Soc*. **2009**, *131*, 8730–8731.

16- D. G. H. Hetterscheid and J. N. H. Reek, *Chem. Commun.* **2011**, *47*, 2712–2714.

17- R. Lalrempuia, N. D. McDaniel, H. Müller-Bunz, S. Bernhard and M. Albrecht, *Angew. Chem. Int. Ed*. **2010**, *49*, 9765–9768.

18- F. Liu, T. Cardolaccia, B. J. Hornstein, J. R. Schoonover and T. J. Meyer, *J. Am. Chem. Soc*. **2007**, *129*, 2446–2447.

19- J. Mola, E. Mas-Marza, X. Sala, I. Romero, M. Rodriguez, C. Viñas, T. Parella and A. Llobet, *Angew. Chem. Int. Ed*. **2008**, *47*, 5830–5832.

20- R. Zong and R. P. Thummel, *J. Am. Chem. Soc*. **2005**, *127*, 12802–12803.

21- T. Wada, K. Tsuge and K. Tanaka, *Angew. Chem. Int. Ed. Engl*. **2000**, *39*, 1479–1482.

22- J. J. Concepcion, J. W. Jurss, P. G. Hoertz and T. J. Meyer, *Angew. Chem. Int. Ed*. **2009**, *48*, 9473–9476.

23- J. D. Blakemore, N. D. Schley, G. W. Olack, C. D. Incarvito, G. W. Brudvig and R. H. Crabtree, *Chem. Sci*. **2011**, *2*, 94–98.

24- N. D. Schley, J. D. Blakemore, N. K. Subbaiyan, C. D. Incarvito, F. D'Souza, R. H. Crabtree and G. W. Brudvig, *J. Am. Chem. Soc.* **2011**, *133*, 10473–10481.

25- K. S. Joya and H. J. M. de Groot, *Netherlands Patent Application* no. 2005512, Oct., **2010**.

26- J. D. Blakemore, N. D. Schley, D. Balcells, J. F. Hull, G. W. Olack, C. D. Incarvito, O. Eisenstein, G. W. Brudvig and R. H. Crabtree, *J. Am. Chem. Soc*. **2010**, *132*, 16017–16029.

27- M. Yagi, E. Tomita and T. Kuwabara, *J. Electroanal. Chem*. **2005**, *579*, 83–88.

28- D. J. Wasylenko, C. Ganesamoorthy, M. A. Henderson, B. D. Koivisto, H. D. Osthoff and C. P. Berlinguette, *J. Am. Chem. Soc*. **2010**, *132*, 16094–16106.

29- A. Savini, G. Bellachioma, G. Ciancaleoni, C. Zuccaccia, D. Zuccaccia and A. Macchioni, *Chem. Commun.* **2010**, *46*, 9218–9219.

30- J. J. Concepcion, J. W. Jurss, J. L. Templeton and T. J. Meyer, *J. Am. Chem. Soc.* **2008**, *130*, 16462–16463.

Appendix A5

[(bpy)-Ir^{III}-(Cp*)Cl]Cl

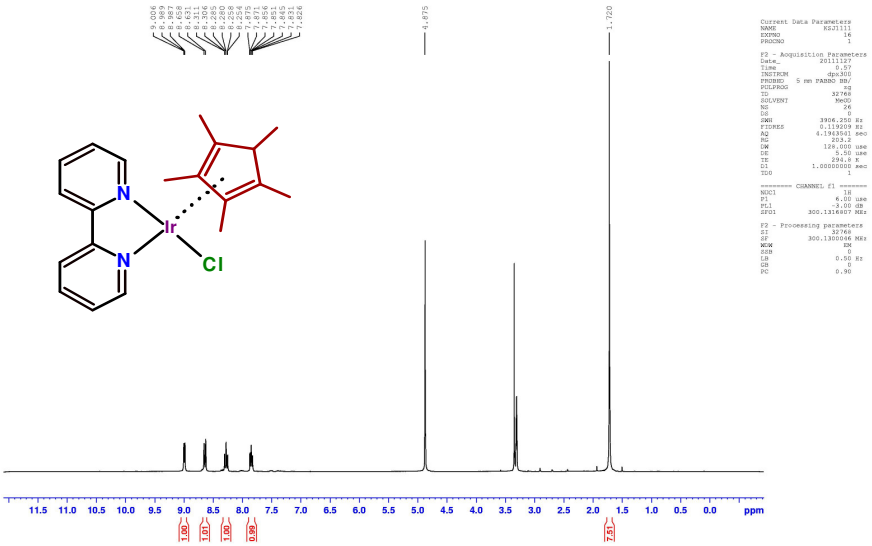

[(phen)-Ir^{III}-(Cp*)Cl]Cl

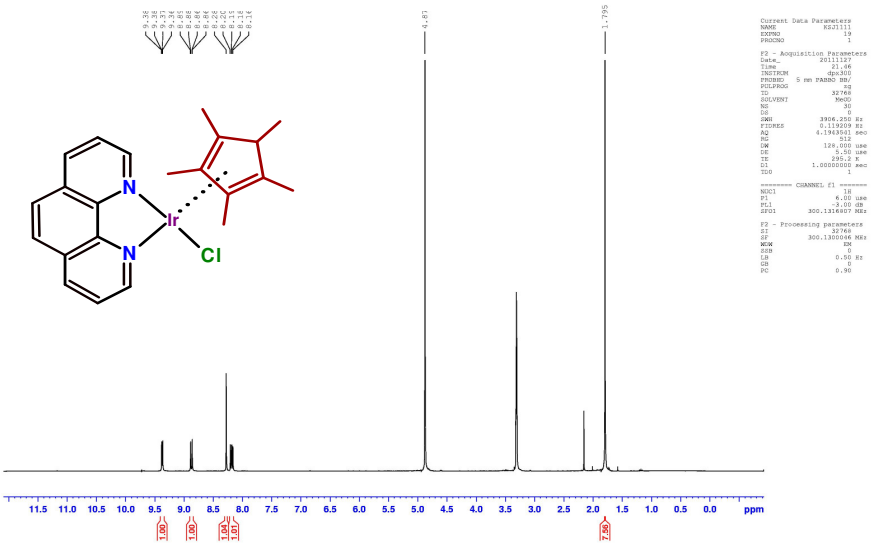

[(bpm)-Ir^{III}-(Cp*)Cl]Cl

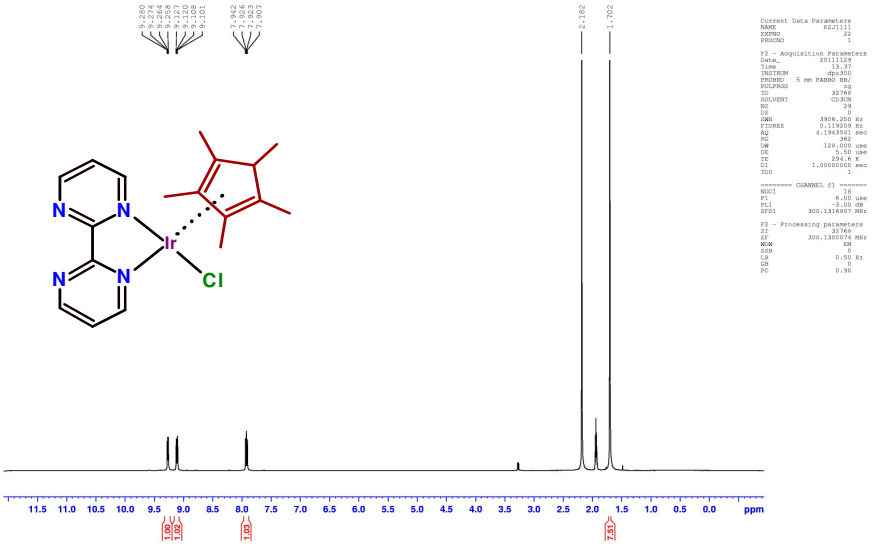

[{$(COOH)_2$-bpy}-Ir^{III}-(Cp*)Cl]Cl

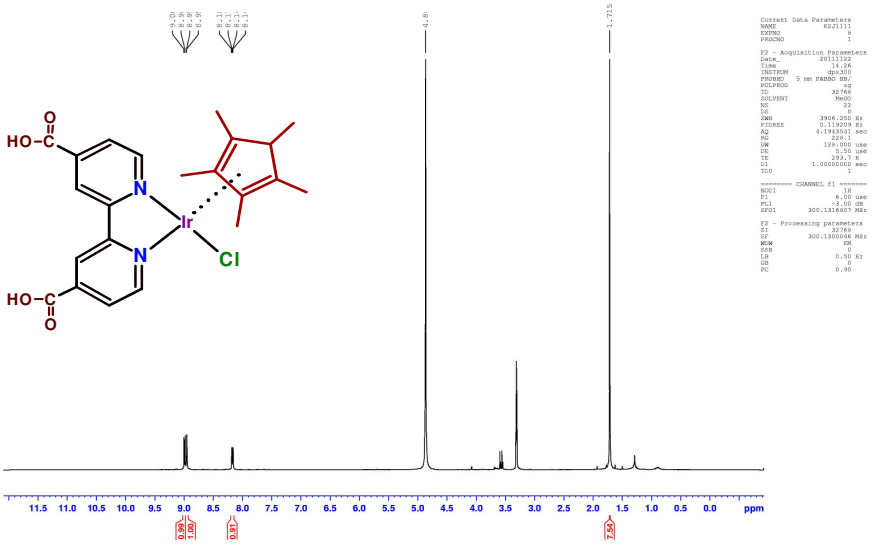

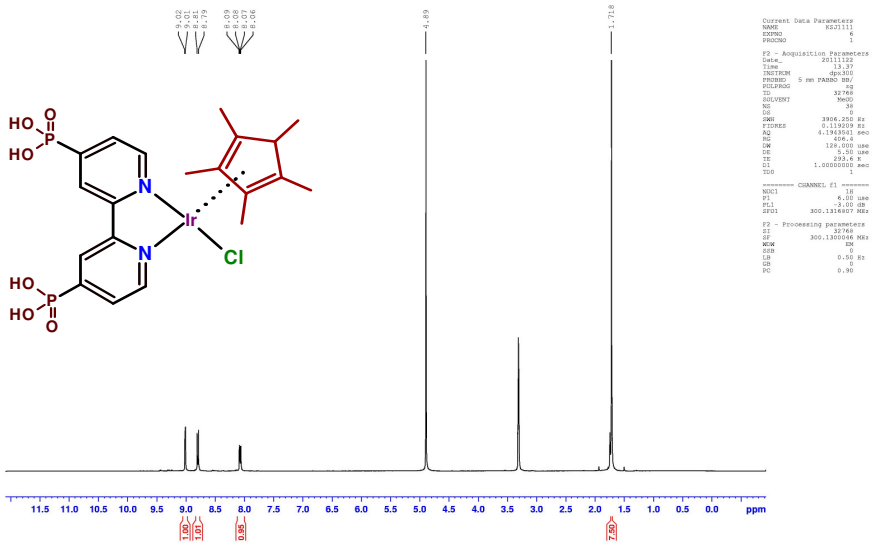

Figure A5.1. Proton NMR spectra of **Ir**-bpy, **Ir**-phen and **Ir**-bpm complexes and linker modified **Ir**-COOH and **Ir**-PO_3H_2 complexes.

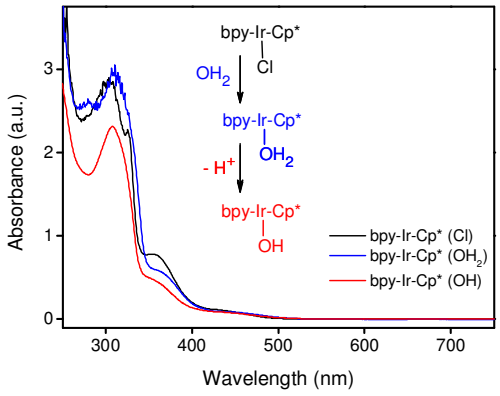

Figure A5.2. Electronic absorption spectra of $[(bpy)Ir(Cp^*)-(Cl)]^+$ complex (black line) following blue curve ascribed to the formation of aqua catalyst $[(bpy)Ru(cy)-(OH_2)]^{2+}$ induced by OH_2 exchange and deprotonation of the aqua catalyst to form $[(bpy)Ru(cy)-(OH)]^+$ complex (red line). For all measurements a concentration of the complex of 7.5×10^{-5} M was used.

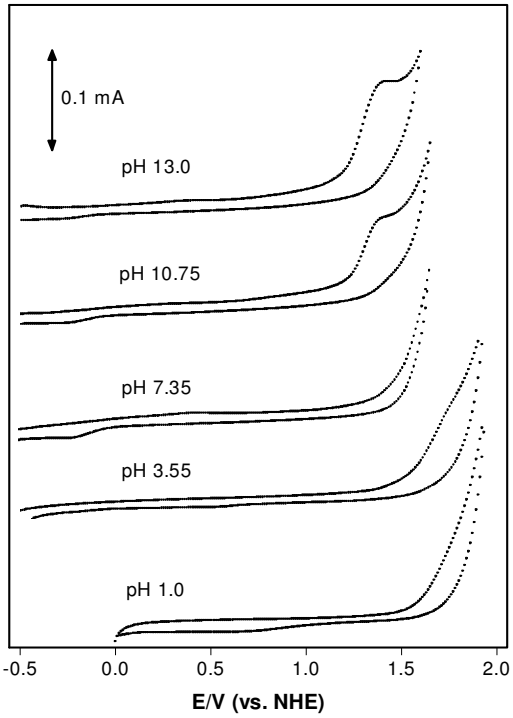

Figure A5.3. Cyclic voltammetry for $[(H_2dcabpy)\text{-}Ir^{III}(Cp^*)]^{2+}$ complex in 0.1 M deoxygenated aqueous solutions with different pH at glassy carbon disk working electrode (WE). Catalyst concentration was 2.5 mM in all experiments, scan rate was 50 mV/sec and the glassy carbon disk diameter was d=5mm.

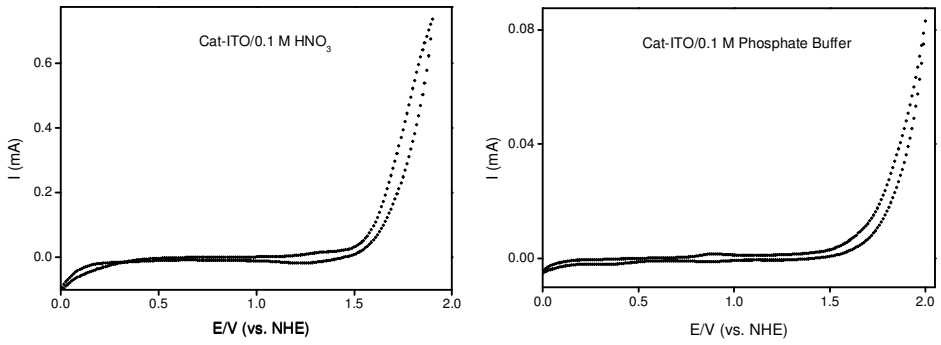

Figure A5.4. Cyclic voltammetry for the $[(L_2bpy)\text{-}Ir^{III}\text{-}(Cp^*)]^{2+}$ complex anchored on an ITO electrode in deoxygenated aqueous (left) 0.1 M HNO_3 (and) 0.1 M phosphate buffer solution pH ~ 7.35. (Scan rate: 50 mV/sec. ITO area A= 1 cm^2).

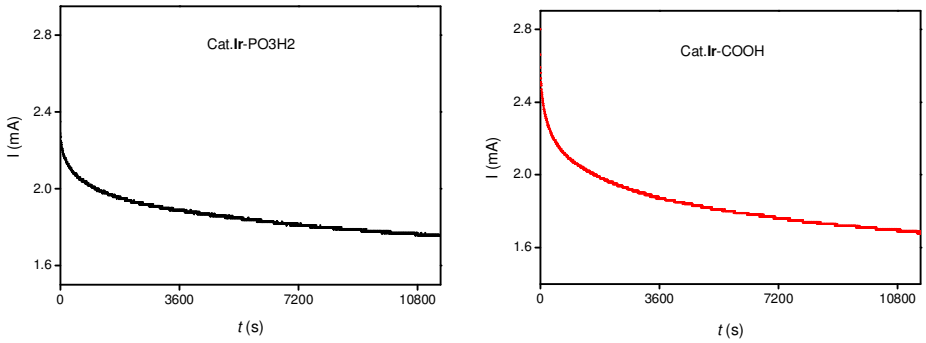

Figure A5.5. Initial oxygen evolution current (3 hrs) during controlled-potential water electrolysis with the (left) Cat.**Ir**–PO_3H_2 and (right) Cat.**Ir**–COOH modified ITO electrodes in deoxygenated buffer (pH=4) solution at *ca*. 1.75 V (vs. NHE), ITO area A=1 cm^2, (catalyst loading ~1.55–1.70 × 10^{-10} mol/cm^2), average initial current density >1.7 mA/cm^2.